ACS APPLIED MATERIALS & INTERFACES

Research Article

www.acsami.org

Surface Characterization for Ultrahigh Molecular Weight Polyethylene/Hydroxyapatite Gradient Composites Prepared by the Gelation/Crystallization Method

Xiaomei Shi, Yuezhen Bin,* Daishui Hou, and Masaru Matsuo*

Department of Polymer Science and Materials, School of Chemical Engineering, Dalian University of Technology, Dalian 116024, People's Republic of China

ABSTRACT: To establish implant longevity of hip prosthesis in orthopedics, a new approach was proposed to improve dramatically the wear resistance and to reduce the surface friction of the acetabular cup as a bearing material in the femoral head. To do so, ultrahigh molecular weight polyethylene (UHMWPE) and hydroxyapatite (HA) composites with four amounts of HA content were prepared by a sol−gel process, and the four composites were hot-molded to make a composite with HA gradient content. When the resultant UHMWPE/HA agglomerates by the sol−gel method were molded in the narrow temperature range of 145−153 °C, the (110) planes with highest density of atoms in the PE crystal unit were oriented predominantly parallel to the resultant film surface. Such an unusual planar orientation contributed excellent wear resistance and low friction on the surface. Polarized light-scattering patterns, SEM images, and FTIR spectra of the specimens with such unusual planar orientation supported that the narrow molding temperature range achieves good dispersion of HA particles and high crystallinity of the UHMWPE matrix on the surface layer. Negative complex Poisson's ratio reduced from complex tensile and shear moduli was attributed to spongy-like tissue formation under crystallization of UHMWPE chains on the HA particle surface. The gradient composite molded maintained the spongy-like structure, which played an important role to avoid the cracking under bending stress.

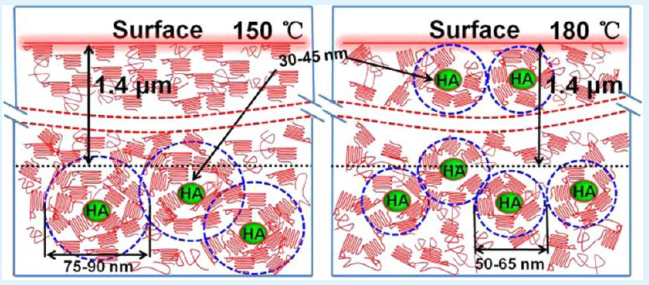

KEYWORDS: *hydroxyapatite composite, gradient composite, sol−gel techniques, hip replacement prosthesis, excellent wear resistance and low friction*

1. INTRODUCTION

Ultrahigh molecular weight polyethylene (UHMWPE) has been used in orthopedics as a bearing material in artificial joints[1−4] because of notable properties such as chemical inertness, lubricity, impact resistance, and abrasion resistance. However, wear damages of the UHMWPE have been one of the factors limiting implant longevity.[5,6] That is, the resultant wear of polyethylene bearing purportedly produces billions of wear particles with submicrometer size that cause adverse pathological reaction in the surrounding tissues leading to osteolysis and joint loosening.[7] The recent wear tests have indicated that the wear resistance of UHMWPE can be improved by cross-linking with desirable gamma irradiation, but the radiation does not bring any good to mechanical properties such as tensile strength.[8]

Hydroxyapatite (HA) is one of the bioceramics with good bioactivity, but the brittle nature has limited the scope of clinical application. Tough composites with bioactivity have the advantage of overcoming the problems of brittleness while maintaining the bioactivity.[9−13] On the basis of this concept, a number of methods have been proposed for the preparations of UHMWPE/HA composites by solid-state mixing, thermal forming,[14,15] compounding HA particles and UHMWPE in paraffin oil using twin-screw extrusion, and subsequently compression molding.[16,17] These methods, however, are difficult to allow uniform dispersion of HA powders in the UHMWPE matrix because of the extremely high melt viscosity of UHMWPE.

In the present work, the gelation/crystallization method by using paraffin with nontoxic property as a solvent is adopted to prepare UHMWPE/HA composites since the high viscosity of UHMWPE solution is helpful to provide a shear stress ensuring uniform dispersion of HA particles. Such a phenomenon was demonstrated for the systems of UHMWPE/carbon black,[18] UHMWPE/carbon fiber,[19] and UHMWPE/multiwall carbon nanotubes (MWCNTs).[20,21] By extraction of paraffin in hexane surrounded by an ice−water bath and the drying, the resultant dry UHMWPE/HA agglomerates were molded as a film under 3 MPa pressure in temperature range 143−180 °C. After thoroughly reviewing data, it becomes clear that the surface of the composites molded in the very narrow temperature range, 145−153 °C, provides an enormous advantage as an acetabular cup. Thus, the surface of the resultant composites assured better wear resistance and friction than well-known

Received: December 10, 2012
Accepted: February 15, 2013
Published: February 15, 2013

 © 2013 American Chemical Society

UHMWPE/HA composites prepared by a kneading method. Accordingly, the present UHMWPE/HA composites indicate notable properties for implant longevity of hip prosthesis in orthopedics.

To understand the enormous advantages, this paper focuses on three factors: (1) planar orientation of the (110) plane with the highest crystal modulus and the highest density among the crystal planes parallel to the *c*-axis, (2) the gelation/crystallization mechanism of UHMWPE chains on the specimen surface estimated for scissoring vibration of $\delta(CH_2)$ by attenuated total reflection (ATR) as well as by statistical analysis of polarized small-angle light-scattering (SALS) patterns, and (3) merits of sponge-like tissues of the gradient composite estimated by Poisson's ratio.

On the basis of the above issue, the gradient composites were prepared to prevent cracking at the bending strain beyond 4%, in which the four kinds of composite film with different HA contents were overlapped and pressed at 150 and 180 °C to prepare gradient composites. The schematic diagram is shown in Figure 1(d). The overlapped film was simulated to prepare

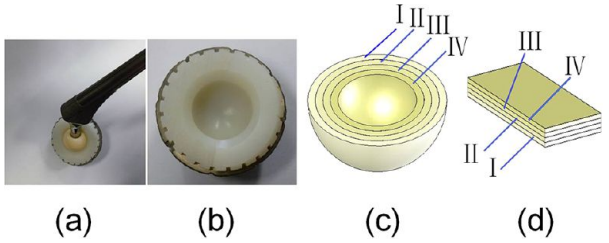

Figure 1. (a) Hip prosthesis in orthopedics used for operation, (b) acetabular cup as a bearing material in the femoral, (c) a model of gradient composite of the acetabular cup, and (d) gradient composite used in the present experiment.

the gradient acetabular cup (Figure 1(c)), which is based on the real artificial hip joint used for operation shown as Figure 1(a) and (b) (no gradient phase). The main concept is focused on the fact that the gradient composite molded at 150 °C was much better than that molded at 180 °C as bearing materials with high wear resistance and smooth surface.

The gradient structure in Figure 1(d) was introduced to avoid the cracking under bending stress because gradations in microstructure and/or porosity are commonly seen in biological structures such as bamboo, plant stems, and bone, where the strongest elements are located in regions that experience the highest stresses.[22] Gradient structure, which helps to redistribute stress and increase damping,[23] is discussed experimentally and theoretically in terms of the temperature dependence of complex Poisson's ratio ν^* reduced from complex tensile moduli E^* and complex shear moduli G^*.[24] The negative value of ν^* is discussed in relation to the spongy-like structure observed by scanning electron microscopy (SEM) and analyzed by the statistical approach[25−27] of polarized Hv light scattering patterns.

2. MATERIALS AND METHODS

2.1. Materials and Preparation of UHMWPE/HA Gradient Composites. UHMWPE was kindly provided by Ticona U.S. with an average viscosity molecular weight of 3×10^6. UHMWPE was purified by Soxhlet extraction by ethanol for 12 h. HA powders ($MH\text{-}HAPO_3$) with an average size of 200 nm were purchased from Nanjing Emperor Nano Material Co., Ltd., China. The purity of HA was 97.5%. Four amounts of HA content against UHMWPE were chosen to be 0 vol %, 13.3 vol %, 23.5 vol %, and 31.5 vol % in preparing the homogeneous UHMWPE/HA dispersion solution. The concentration of UHMWPE was set to be 1 g/100 mL with respect to the solvent. By using a successful method for MWCNT,[18−21,28,29] a uniform dispersion of the HA powders into paraffin solutions could be achieved by alternate ultrasonic and stirring for more than 12 h at room temperature. After that, UHMWPE powder was added into the dispersed solvent containing the HA, and the mixture was stirred at room temperature for 1 h. Under stirring by screw, the mixture was heated to 145 °C and was maintained for 30 min at the same temperature. Then the UHMWPE/HA dispersion solution was extracted by hexane in an ice−water bath. The resultant UHMWPE/HA agglomerates were dried at 60 °C in a hot oven after the extraction. After drying, the agglomerates were pressed to prepare the composite film at a fixed temperature in the range of 143−180 °C under the pressure of 3 MPa for 15 min. Furthermore, the gradient composite of UHMWPE/HA as shown in Figure 1(d) was prepared by overlapping and pressing the four composite films with 0 vol %, 13.3 vol %, 23.5 vol %, and 31.5 vol % together at 150 or 180 °C under 3 MPa.

Suitable different sample thickness was selected for various measurements, but the value of the gradient composite must be set to be the same as the values of the composites with different HA contents, for example, when the thickness of each resultant molded composite was selected to be ca. 0.2 mm and the gradient composite thickness must be ca. 0.2 mm, in which the thickness of each composite layer to overlap was ca. 0.05 mm, that is, $0.05 \times 4 = 0.2$ mm. The molding was done in a cupper frame covered by clean cupper plates. The displayed temperature in the hot press instrument was confirmed to be equivalent to the temperature of the molding plate, which is also thought to be equal to the polymer's temperature.

2.2. Phase and Microstructural Analysis. *Sacnning Electron Microscopy (SEM) Observation and the Energy Dispersion X-ray Spectrometry (EDS) Spectra.* SEM observation was carried out by QUANTA 450 by coating chromium on the agglomerates. The chromium thickness is ca. 10 nm. Energy dispersion X-ray spectrometry (EDS) (Oxford Instruments X-Max) was used to analyze atomic elements of HA agglomerates and UHMWPE/HA agglomerates under observation of SEM at 20 kV.

Before investigating surface characterization of the UHMWPE/HA composites, SEM and EDS supplemental experiments were carried out in Figures 2−4.

To take SEM image (a) in Figure 2, the HA agglomerates were treated by alternative ultrasonic and stirring at room temperature as discussed before. By the treatment, the sizes of the HA agglomerates were 30−45 nm, indicating cutting of the original narrow HA particles, the average long length being ca. 200 nm, by ultrasonic treatment and screw stirring. The treated HA particles and UHMWPE/HA agglomerates with 23.5 vol % HA content after the drying were adopted. Image (b) shows the UHMWPE/HA agglomerates (before the molding). The sizes of the HA agglomerates were 30−45 nm. The sizes were 90−95 nm. Because of the large different domain sizes between images (a) and (b), the surfaces of HA agglomerates were obviously covered by UHMWPE layers as like MWCNT.[28,29] A similar structure was confirmed for the UHMWPE/HA agglomerates with 31.5 vol % HA content.

To demonstrate the covering decisively, EDS are shown in columns (c) and (d). The EDS spectrum (c) of HA particles shows a normal profile, and the contents of the atomic elements are listed in the frame. The spectrum (d) of the UHMWPE/HA agglomerates with 23.5 vol % HA content shows the summation of PE and HA since the carbon element listed in spectrum (d) is much higher than that of spectrum (c). Obviously, this indicates that the surfaces of HA agglomerates were covered by UHMWPE layers since the clear peaks for Ca and P elements can be observed in spectrum (d). The atomic elements listed in frames (c) and (d) indicate the covering of UHMWPE on the HA surface clearly.

Figure 3 shows that image (a) shows HA agglomerates with the diameter of 30−45 nm, and image (b) shows UHMWPE/HA agglomerates with 23.5 vol % HA melted at 220 °C for 30 min. As shown in image (b), most of the melted UHMWPE chains were

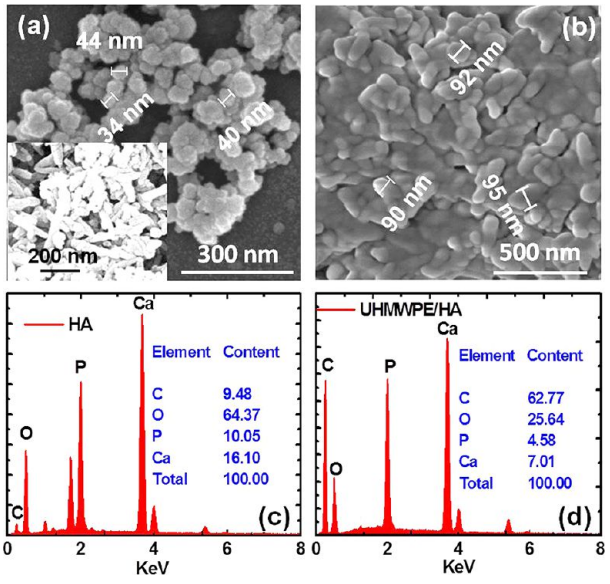

Figure 2. (a) SEM picture of HA agglomerates, (b) UHMWPE/HA agglomerates with 23.5 vol % HA content, (c) EDS spectrum for HA agglomerates, and (d) EDS spectrum of UHMWPE/HA agglomerates with 23.5 vol % HA content. The inset in (a) shows the original HA powders.

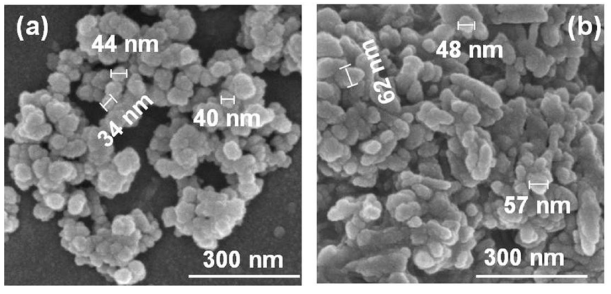

Figure 3. SEM photographs of the HA and UHMWPE/HA agglomerates. (a) HA agglomerates and (b) UHMWPE/HA agglomerates with 23.5 vol % HA content after melting at 220 °C for 30 min.

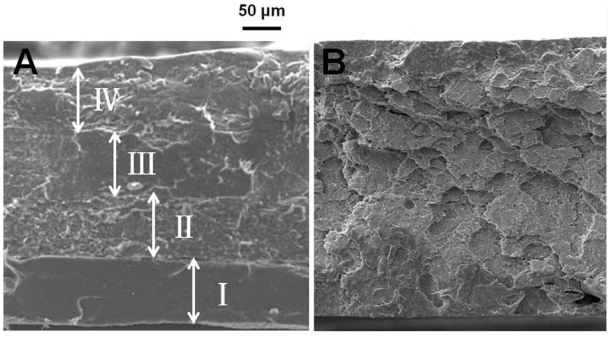

Figure 4. SEM photographs of gradient UHMWPE/HA composites. (A) Molded at 150 °C: I, 0 vol %; II, 13.3 vol %; III, 23.5 vol %; IV, 31.5 vol %. (B) Molded at 180 °C.

flowed off from the HA surface. However, melted UHMWPE chains remained on the HA surface, and the remaining UHMWPE chains were recrystallized on the HA surface. Consequently, the diameter 45–65 nm of the UHMWPE/HA agglomerates melted at 220 °C is much smaller than the diameter 90–95 nm of the corresponding agglomerates before the melting (see Figure 2(b)) but is slightly larger than the diameter 30–45 nm of the HA agglomerates shown in Figure 3(a). The flowed off UHMWPE chains from the surface of the HA agglomerate play a role in adhering adjacent UHMWPE/HA agglomerates.

Figure 4 shows the cross-section of the graded structures of the composites layers molded at 150 and 180 °C. To observe the cross-section of the composite film, the film was put into liquid nitrogen, and the frozen film was cracked by hand to observe the fractured surface of the samples. Then, chromium was coated on the surface. Each thickness of the four composite layers to make the gradient composite was 0.05 mm, and the thickness of the gradient composite was 0.2 mm. At 150 °C, SEM image (A) shows the clear boundary layers with different HA contents. On the other hand, at 180 °C, SEM image (B) shows unclear boundary lines of the layers with different HA contents because of partial melt-flowing of UHMWPE (mainly from layer I). The two gradient composites molded at 150 and 180 °C revealed quite different structures.

2.3. Thermal Property Analysis. The differential scanning calorimeter (DSC) measurements were performed on about 5–10 mg of sample sealed in aluminum pans by a DSC-204 (NETZSCH) at a heating rate of 10 °C/min under N_2 atmosphere. To pursue smooth discussion about surface characterization of UHMWPE/HA composites, DSC results are added as supplemental experiments.

Figure 5(a) shows DSC results for UHMWPE/HA agglomerates, and (b) and (c) show the DSC curves for the composites molded at 150 and 180 °C, respectively. The measurements were done three times for the same kinds of specimen, but the observed profiles were almost the same. As can be seen in DSC curves, the endothermic peaks appeared in the range from ca. 130 to ca. 142 °C. The endothermic peak by molding shifted to the lower temperature side in comparison

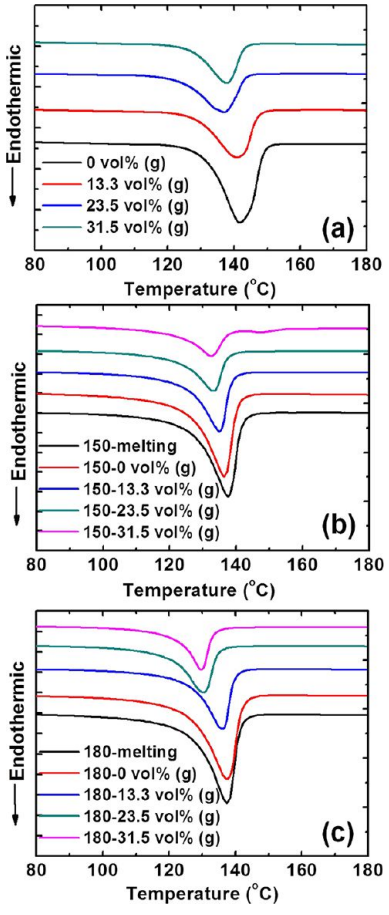

Figure 5. DSC curves of the UHMWPE/HA composite with different HA contents. (a) UHMWPE/HA agglomerates (before molding), (b) molded at 150 °C, and (c) molded at 180 °C.

dx.doi.org/10.1021/am3030504 | ACS Appl. Mater. Interfaces 2013, 5, 1768–1780

Table 1. Crystallinity for UHMWPE/HA Agglomerates and the Composites Molded at 150 and 180 °C with Different Content

agglomerate	crystallinity (%)	melted sample	crystallinity (%)	melted sample	crystallinity (%)
		150-melting	53.1	180-melting	56.5
0 vol % (g)	84.5	150-0 vol % (g)	58.8	180-0 vol % (g)	55.1
13.3 vol % (g)	80.1 1	50-13.3 vol % (g)	55.7	180-13.3 vol % (g)	53.7
23.5 vol % (g)	81.7	150-23.5 vol % (g)	56.1	180-23.5 vol % (g)	57.9
31.5 vo l% (g)	82.0	150-31.5 vol % (g)	58.7	180-31.5 vol % (g)	56.4

with the original agglomerates. The right foot of the peak of pristine UHMWPE was ca. 150 °C, which indicated perfect melting occurred at 150 °C. Interestingly, as discussed in Figure 3, it should be noted that UHMWPE did not flow off from the surface of HA agglomerates even at 220 °C perfectly because of the very high viscosity of UHMWPE. Judging from such a phenomenon, most of the melted UHMWPE chains were not flowed off and were recrystallized again on the surface of HA agglomerates in the composite molded at 150 °C. On the other hand, at 180 °C, some of the melted UHMWPE chains were flowed off, and the residual UHMWPE chains were recrystallized again on the surface of HA agglomerates. This shall be discussed later in Figure 14.

With increasing HA content, the endothermic peak top tends to shift to lower temperature. The crystallinities of the composites were evaluated by heat of fusion of each specimen, heat of fusion of 100% PE (280.5 J/g), and volume fraction of UHMWPE.[29] The average values by three trials were listed in Table 1.

As listed in Table 1, the crystallinity of UHMWPE covered on the HA surface was beyond 80%, but the high crystallinity of original UHMWPE/HA agglomerates decreased drastically by molding at 150 and 180 °C. These results were the average value for the three measurements. The crystallinity difference between 150 and 180 °C is not noticeable. This suggested that the crystallinity was not accelerated by recrystallization under the cooling process after heat melting. The supplemental DSC results shall be discussed in relation with wide-angle X-ray diffraction (WAXD), attenuated total reflection (ATR), and small-angle light-scattering (SALS) results shown later.

2.4. Mechanical and Tribological Characterization. The sliding wear of the samples was measured by using a friction and wear experimental machine (M-2000 A) under dry station (as shown in Figure 6(a)).[30,31] The sliding pair consisted of a tested sample

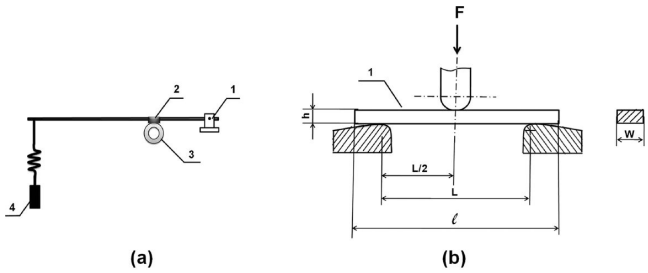

Figure 6. (a) Schematic diagram of the friction tester: (1) support axes, (2) test specimen, (3) steel ring, (4) weight. (b) A schematic diagram of bending tester: (l) length of test specimen; (h) thickness of test specimen; (F) applied force; (L) length of span between supports; (W) width of the test specimen.

(UHMWPE/HA) block and a steel ring, in which the upper side was the sample and the lower side was the steel ring. The external and inner diameters of the ring were 40 and 16 mm, respectively. The counter surface of the ring was polished to the roughness Ra 0.8 μm. Under normal load up to 1200 N, the sliding was achieved by the rotation of 45 steel ring with the sliding speed of 0.42 m/s corresponding to the axis rotation speed of 200 rpm. The sliding time was 3 h, and the tests were done more than three times for each sample to ensure reproducibility. The average coefficient was measured at the ring rotation more than 10 000 cycles, ensuring a stable sliding stage.

The wear rate was calculated by volume loss of per sliding distance as follows[31]

$$\omega = \frac{\Delta W}{2\pi\rho RN} \quad (1)$$

In eq 1, ω represents the wear rate (mm^3/m), ΔW the mass loss (g), ρ the density of the sample (g/mm^3), R the radius of the counterpart (steel ring) (m), and N the number of rotations. The friction coefficient μ was calculated by

$$\mu = \frac{T}{RP} \quad (2)$$

where T and P are the friction torque (Nm) and the normal load (N), respectively.

Shallow dent shapes by the wearing were estimated by Talysurf PGI 1240, in which the sliding speed of the point was 0.2 mm/s.

Bending tests were carried out by using INSTRON-5567A (American Instron company) for a specimen 40 mm long, 3 mm wide, and with 2 mm thickness at the speed of pressure head 2 mm/min.[32] The gradient composite with 2 mm thickness was prepared by hot-pressing the four overlapped composite layers with 0.5 mm thickness (0.5 mm × 4 = 2 mm). The well-known schematic diagram to measure bending strength was shown in Figure 6(b).[32] The calculation was carried out by the flexural-stress parameters defined using the following equation

$$\sigma_f = \frac{3FL}{2bh^2} \quad (3)$$

where σ_f is the flexural-stress parameter, which is given by F (the applied force (N)), L (span length (mm)), b (specimen width (mm)), and h (specimen thickness (mm)).

Complex Dynamic Tensile Modulus and Shear Tests. The complex dynamic tensile modulus E^* was measured at 10 Hz in the temperature range from −146 to 130 °C by using a visco-elastic spectrometer (VES-F) (Iwamoto Machine Co. Ltd.). The length of the specimen between the jaws was 30 mm, and the width was about 4 mm. The external strain was 0.002 mm. The complex shear modulus G^* was measured in the temperature range from 20 to 140 °C at a heating rate of 3 °C/min under initial strain of 0.01% by using a Rheometer (AR 2000ex) with an oscillation temperature ramp method at TA Instruments company. The length, width, and thickness of each specimen were 60 mm, 10 mm, and 2 mm, respectively.

2.5. Structural Property Analysis. *Small-Angle Light Scattering (SALS).* Small-angle light scattering (SALS) under Hv polarization condition was observed with a 3 mW He−Ne gas laser as a light source. The observation method was described elsewhere.[33]

Wide-Angle X-ray Diffraction (WAXD). Diffraction peak profiles for UHMWPE/HA composite films were measured by a transmission method with a 12 kW rotating-anode X-ray generator (Rigaku RDArA), in which WAXD intensity measurements were carried out using a step-scanning method with a step interval of 0.1°, each at a fixed time of 40 s, in the range from 10 to 35°. The X-ray instrument was operated using Cu K_α radiation (λ = 0.1542 nm) at l50 mA and 40 kV. The incident beam was monochromatized by a curved graphite monochromator.[34] The film thickness of each composite was 0.2 mm.

Attenuated Total Reflection (ATR). Attenuated total reflection (ATR) measurements were performed by a NEXUS FTIR spectrometer. All spectra in the range 675−4000 cm^{-1} were obtained from a total reflection mold with 2 cm^{-1} spectral resolution, in which the penetration depth d_p of the evanescent wave is given by[35−38]

$$d_p = \frac{\lambda}{2\pi n_1 \sqrt{\sin^2 \alpha - n_{21}^2}} \quad (4)$$

where λ is the wavelength of the incident radiation; α is the angle of incidence measured from the normal to the surface; $n_{21} = n_2/n_1$ with $n_1 > n_2$, where n_2 is the index of the sample, which is assumed to be 1.5; and n_1 is the refractive index of the optical material (KRS5 = 2.38). In the present experiment, α was fixed to be 45°. The film thickness of each composite was 0.2 mm.

3. RESULTS AND DISCUSSION

Figure 7(a) and (b) shows a frictional coefficient against the normal load for the composites molded at 150 and 180 °C,

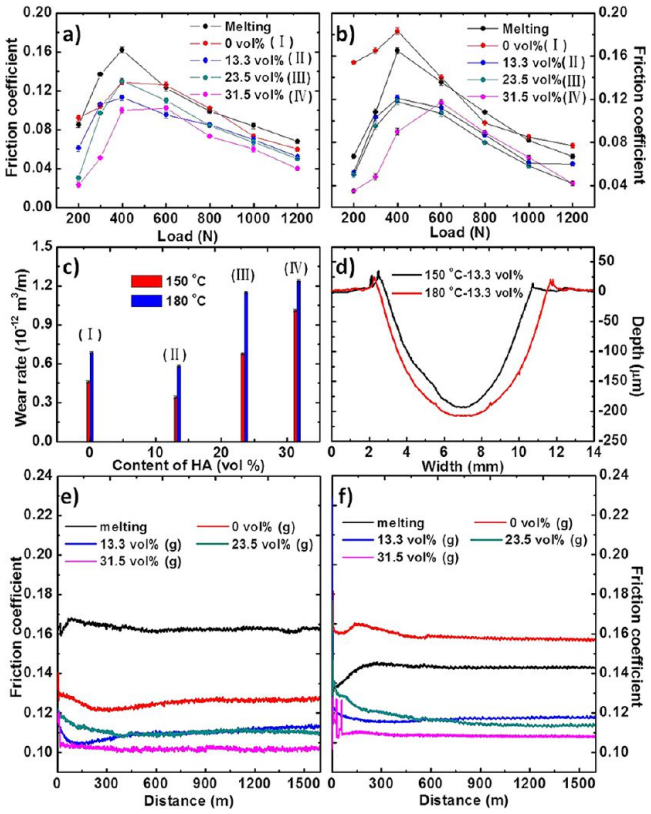

Figure 7. (a) and (b) Friction coefficient of UHMWPE/HA composites molded at 150 and 180 °C, respectively. Each error bar is very small, indicating high accuracy. (c) Wear rate of the UHMWPE/HA composite molded at 150 and 180 °C, in which the normal load and the rotating period were 1200 N and 3 h, respectively. (d) The shallow dent shapes by the wearing measurement of (c). (e) and (f) friction coefficient vs the distance traveled during wear for composites molded at 150 and 180 °C, respectively.

respectively. Figure 7(c) and (d) shows the corresponding wear rates and shallow dent shapes by the wearing, respectively. As shown in Figure 7(a) and (b), the frictional coefficient increases with normal load, but beyond the maximum point, it decreased. Such behavior has never been reported, but it plays an important role in ensuring sufficient smooth movement of hip prosthesis beyond 400 N when subjecting to the shock load. The descent tendency beyond 400−600 N is probably thought to be due to an acceleration of the surface smoothness by a heavy normal load.

As a whole, the frictional coefficient becomes slightly lower with increasing HA content, which indicates an advantage to using the composite with 31.5 vol % HA content as the inner layer (IV) in Figure 1(c) (or (d)).

Here, two questions can be arisen: (1) why the friction coefficient becomes lower with increasing HA content and (2) why the maximum peak for 31.5% HA content shifted to 600 N. As the first, the intrinsic fraction of pristine HA becomes lower than that of UHMWPE, but there is no method to measure the intrinsic friction of pristine HA directly. Even so, the same tendency for the composites was reported already.[39,40] As the second, the peak shift of the friction coefficient with increasing normal load is obviously related to the disappearance of the number of voids within the sponge-like structure composites, which shall be discussed in relation to Poisson's ratio later in Figure 17.

Judging from adverse pathological reaction in the surrounding tissue by UHMWPE powder, the composite with 31.5 vol % HA content is obviously favorable as the inner layer. By considering the heavy weight of the trunk of the human body, the wear rate against HA content in Figure 7(c) was estimated after sliding for 3 h under normal load of 1200 N. The wear rate is slightly higher with increasing HA content, but the important factor is HA content with nontoxic property contained in the wearing powder. Obviously, layer IV prepared by molding at 150 °C plays an important role in restricting amounts of scattering UHMWPE wear particles. However, the further improvement for wear rate must be considered.

The corresponding wear shapes, for example, are shown for the composites with 13.3 vol % HA content in Figure 7(d), which is not symmetrical, reflecting nonuniform grinding of the composites by rotation. Even so, the wear depth by the grinding for the composite molded at 150 °C is shallower than that at 180 °C, indicating better abrasion resistance. Of course, the fraction of pristine UHMWPE prepared by gelation/crystallization and molded at 150 °C is slightly better than that prepared by the kneading (melting) method. Figure 7(e) and (f) shows the fraction coefficient as a function of distance traveled during wear up to 1500 m for the composites molded at 150 and 180 °C, respectively. The friction coefficients as a function of distance up to 1500 m are constant except the initial stage, and the values for the composite molded at 150 °C are slightly lower than that at 180 °C. The results obviously suggest that the composite with 31.5% HA content is suitable as the surface layer (IV) of the gradient composite on the viewpoint of surface smoothness.

Figure 8 shows bending stress vs bending strain for the pristine UHMWPE, UHMAWP/HA composites, and the gradient composite molded at 150 and 180 °C, and a series

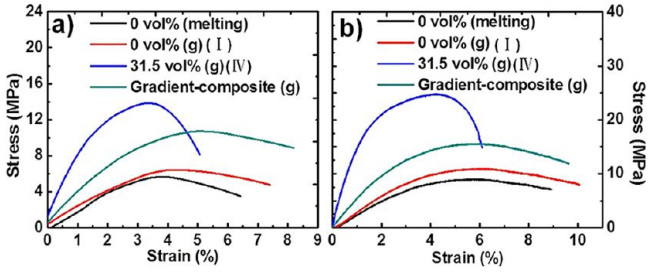

Figure 8. Bending stress and strain for UHMWPE films prepared by melting (m) and gelation (g), UHMWPE/HA dry gel composite with 31.5 vol % HA content, and dry gel gradient composite shown in Figure 1(d). They were molded at 150 °C (a) and 180 °C (b).

dx.doi.org/10.1021/am3030504 | ACS Appl. Mater. Interfaces 2013, 5, 1768−1780

Table 2. Flexural Yield Stress, Yield Strain, Maximum Strain, and Flexural Modulus for the Indicated Specimens Molded at 150 and 180 °C, in Which the Specimens Were Prepared by Melting or Gelation/Crystallization

		flexural yield stress/MPa	yield strain/%	maximum strain/%	flexural modulus/MPa
melting (0 vol %)	150 °C	5.65	4.06	6.42	200.39
	180 °C	9.11	5.42	8.93	273.73
gelation/crystallization (0 vol %)	150 °C	6.44	6.32	7.39	217.4
	180 °C	12.19	6.35	10.07	322.89
gelation/crystallization (31.5 vol %)	150 °C	13.85	3.4	5.07	683.26
	180 °C	23.84	4.1	6.10	1725.87
gelation/crystallization composite	150 °C	10.73	5.04	8.19	352.43
	180 °C	14.6	5.94	9.62	550.74

of flexural stress and strain values obtained from Figure 8 are listed in Table 2. The measurements were carried out five or six times for the same kinds of specimens, and the representative curve among the three or four curves was selected after eliminating the unusual curves by sample defects. With increasing HA content, the flexural yield (maximum) stress increased, while flexural yield strain at yield (maximum) stress decreased. The flexural yield stress was the highest for the composite with 31.5 vol % HA content, but the flexural yield strain was the lowest. This suggests that the acetabular cup prepared by 31.5 vol % HA content shall be brittle for large displacement, although the friction coefficient is the lowest as shown in frames (a) and (b) in Figure 7. The advantage of the gradient composite is to avoid the cracking under bending stress. Actually, the maximum (up to breaking) flexural strain and flexural yield strain of the gradient composite were higher than those of the single composite with 31.5 vol % HA content, and the yield stress was higher than that of pristine UHMWPE (layer I). Incidentally, the flexural yield stress and maximum flexural strain (up to breaking) of the pristine UHMWPE prepared by the sol–gel method were higher than those prepared by the kneading (melting) method. This indicates that the UHMWPE/HA composite prepared by the sol–gel method is thought to be the best as an acetabular cup in comparison with methods reported elsewhere.[16,41,42] As a whole, flexural yield stress, flexural yield strain (strain at maximum flexural stress), maximum strain (up to breaking), and flexural modulus of the composites molded at 180 °C were higher than those of the composites molded at 150 °C. Such bending property concerning large deformation was strongly affected by the morphology of UHMWPE/HA agglomerates in the molded composites, which shall be discussed later in relation to small-angle light-scattering patterns in detail.

A series of experimental results in Figure 7 and Figure 8 indicate the advantage of the gradient composites to prepare the acetabular cup. To further investigate the advantageous reason about surface property of the composites molded at 150 °C, X-ray and FTIR measurements were carried out later for pristine UHMWPE films molded in the temperature range 143–180 °C.

Figure 9 shows WAXD intensity distributions from pristine UHMWPE films measured by a transmission method for the films, taking a random orientation of crystallites around the film thickness direction. In columns (b), (c), and (d), the diffraction intensity from the (110) plane is weaker than that from the (200) plane. Such behavior reveals unusual behavior for the specimens molded in the temperature range from 145 to 153 °C. Generally, the diffraction intensity from the (110) plane must be higher than that from the (200) plane, which is due to the well-known fact that the structural factor of the (110) plane

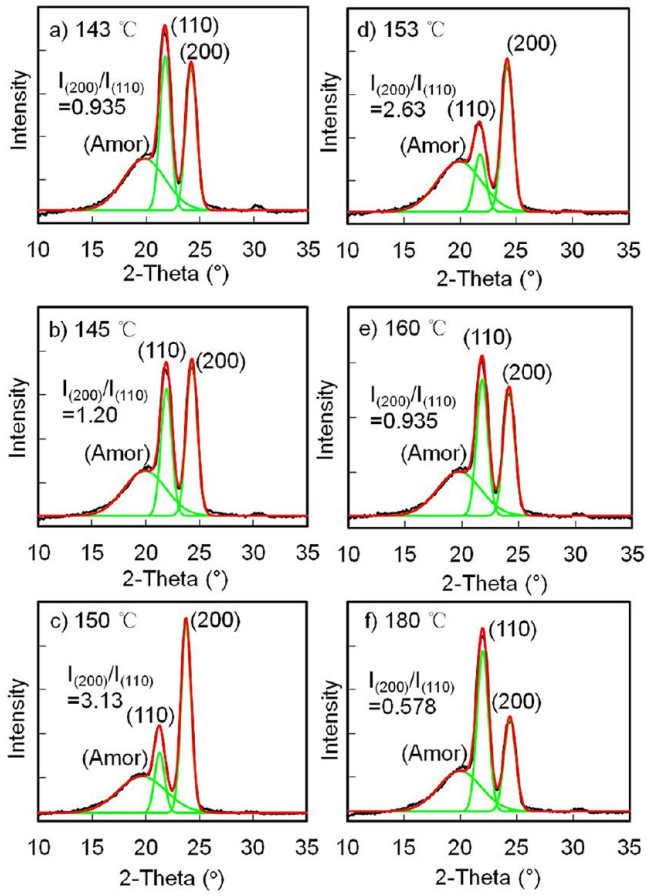

Figure 9. WAXD curves for pristine UHMWPE films molded at the indicated temperatures. In each column, a black curve represents experimental results and the green curves represent individual components of the amorphous, the (110) plane, and the (200) planes. The red curve is total contribution from the three components.

is much higher than that of the (200) plane. Hence, the films molded at 145–153 °C assured the preferential orientation of the (110) plane parallel to the film surface. Such an unusual planar orientation of the (110) plane has never been reported since most of the papers have reported the planar orientation of the (200) plane by simultaneous biaxial stretching, rolling, and extrusion.[43–45]

To investigate the molded temperature dependence on the surface property quantitatively, the peak separation of the X-ray diffraction profile was done by curve fitting using a computer. In each column, the individual separated peaks are represented as green curves for the (110) plane, the (200) plane, and the amorphous phase, and the total intensity of the above three

dx.doi.org/10.1021/am3030504 | ACS Appl. Mater. Interfaces 2013, 5, 1768–1780

components is given as a red curve. The total curve as a summation (red) curve of the three components is in good agreement with the experimental (black) curve. As listed in each frame of Figure 9, the ratio of intensity peak area, $I_{(200)}/I_{(110)}$ for the (200) and (110) planes for the specimens molded at 143, 145, 150, 153, 160, and 180 °C, was estimated to be 0.935, 1.20, 3.12, 2.63, 0.935, and 0.578, respectively. $I_{(200)}/I_{(110)} > 1$ reveals the preferential planar orientation of the (110) plane.

The preferential orientation of the (110) plane realized by molding in the narrow temperature range (145−153 °C) provides an effective advantage for the film surface, since the crystal modulus (4.21 GPa)[46] of the (110) plane estimated by WAXD is higher than that (3.14 GPa)[46] of the (200) plane because of the highest atomic density of the (110) plane among the PE crystal planes. The X-ray curve profile justifies the results of friction and wear rate in Figure 7.

Figure 10 shows FTIR (ATR) spectra from pristine UHMWPE films represented as a black curve in the range 1400−1500 cm^{-1}. The doublet peak bands appearing at 1463 and 1473 cm^{-1} are known as scissoring vibrations of $\delta(CH_2)$ as shown in a schematic PE crystal unit, and the established assignment reported the widths to be 2 cm^{-1} for the *n*-alkanes at room temperature.[35−38] The detailed analysis by the established procedure provided a further two peaks concerning the amorphous phase. The one is the peak band at 1442 cm^{-1} associated with the existence of gauche conformations, and the other is the peak at 1467 cm^{-1}. In the present specimens, the peak appeared at 1457 cm^{-1} instead of 1442 cm^{-1}. On the basis of the two assignments, peak separation by curve fitting provided the green curves for the individual components.

In each column, the total absorption curve of the four individual peaks represented as a red curve is in good agreement with the experimental (black) curve. As shown in Figure 11, the crystallinity (X_c) of penetration depth at ca. 1.4 μm from the film surface, which was estimated by eq 4, was given by using $X_c = (A_{1463} + A_{1473})/(A_{1463} + A_{1473} + A_{1442} + A_{1467}) \times 100(\%)$, in which, for example, A_{1463} denotes the absorption peak area with a peak top at 1463 cm^{-1}. The calculated crystallinities (X_c) were 54.9% at 143 °C, 60.1% at 145 °C, 66.7% at 150 °C, 55.5% at 153 °C, 55.1% at 160 °C, and 55.1% at 180 °C. Interestingly, the crystallinities on the surface layer molded at 145−153 °C were slightly higher than the surface layer crystallinities of the specimens molded at 143, 160, and 180 °C. This is probably thought to be attributed to the predominant planar orientation degree of the (110) plane on the surface layer.

Judging from the results by WAXD and FTIR for pristine UHMWPE films molded at the indicated temperatures, the wear rate is found to be sensitive to the molding temperature of UHMWPE. As discussed before, the frictional coefficient and wear rate at 150 °C which are lower than those at 180 °C (see Figure 7) are attributed to the high preferential orientation of the (110) plane and the high crystallinity on the surface layer.

Meanwhile, the UHMWPE/HA composites provided usual WAXD profiles whose diffraction peak from the (110) plane was much higher than that from the (200) plane, which is different from the planar orientation behavior of the (110) plane of the pristine UHMWPE film in Figure 11(b), (c) and (d). Hence, the usual profiles are not shown as a figure in the present paper. The normal profiles mean that the mixing of HA caused a random orientation for UHMWPE crystallites in the composite. The X-ray diffraction intensity from the (110) and

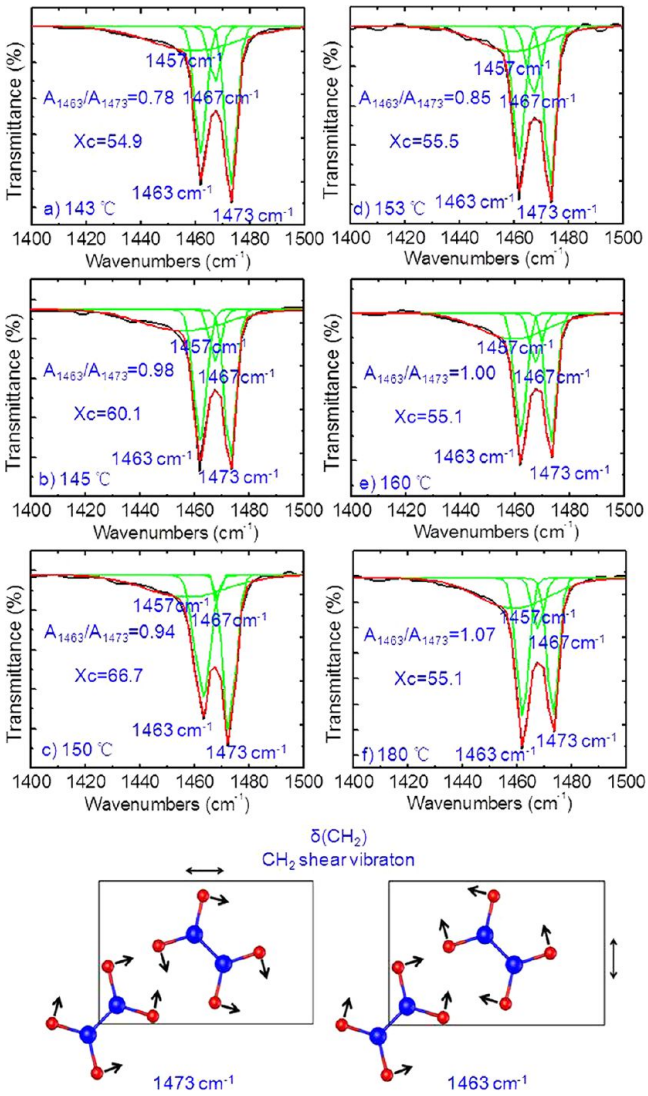

Figure 10. FTIR (ATR) spectra for UHMWPE molded at the indicated temperatures. In each column, the black curve represents experimental results, and the four green curves are associated with scissoring vibrations of $\delta(CH_2)$ at 1463 and 1473 cm^{-1} as shown in the schematic crystal unit and amorphous bands at 1467 and 1442 cm^{-1}. The red curve is total contribution from the four components.

(200) planes became lower with increasing HA content. The diffraction peak from UHMWPE crystallites disappeared for 31.5 vol % HA content, and the strongest peak from the (211) plane of HA crystallites appeared at ca. 31.8°.[11] The X-ray diffraction obtained by the transmission method provides the orientation of crystallites in the entire composite and provides no information only on the surface. The X-ray diffraction of the composites suggested random dispersion of the UHMAPE crystallites by incorporating the HA particles.

Figure 11 shows FTIR spectra of the UHMWPE/HA composites in addition to the bottom FTIR spectrum from HA powder. The absorption peaks at 1463 and 1473 cm^{-1} for UHMWPE/HA composites show profiles similar to pristine UHMWPE film shown in Figure 10. In the range of 1400−1450 cm^{-1}, however, most of the peaks of HA appearing for the composites molded at 150 °C are negligibly small, while the HA peaks for the composite molded at 180 °C are clearer with increasing HA content. Such different ATR spectra provide

dx.doi.org/10.1021/am3030504 | ACS Appl. Mater. Interfaces 2013, 5, 1768−1780

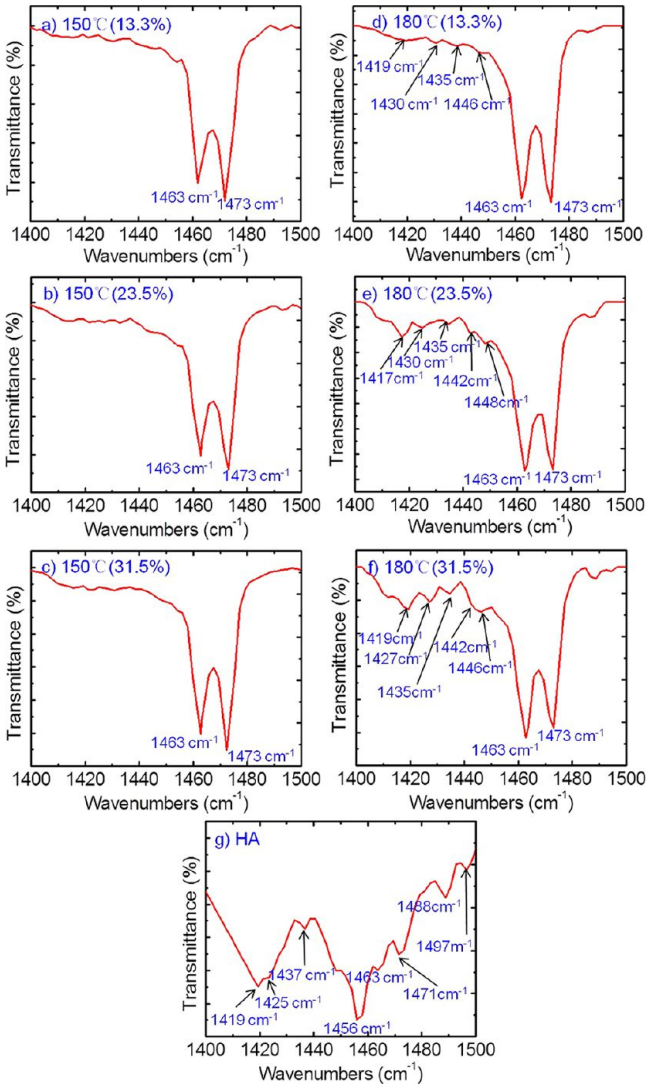

Figure 11. FTIR (ATR) spectra (a–f) for UHMWPE/HA composites molded at 150 °C (left side) and at 180 °C (right side) and the bottom spectrum (g) for HA powders.

important information to justify the different surface morphology dependence for the composites molded at 150 and 180 °C. The difference indicates very few existing possibilities of HA agglomerates on the surface layer (from surface to depth of ca. 1.4 μm) in the composites molded at 150 °C, while enough HA agglomerates dispersed in the thin surface layer in the composites molded at 180 °C. Judging from two factors, (1) very few existing probabilities of HA agglomerates on the surface layer in the composites and (2) the planar orientation of the (110) plane of the pristine UHMWPE film, it may be concluded that planar orientation in the (110) plane is surely maintained on the surface layer (almost no existence of HA particles) of the composites molded at 150 °C and high crystallinity of the thin layer of the composites. Accordingly, this phenomenon provided better wear resistance and surface friction in the composites molded at 150 °C than those molded at 180 °C in Figure 7. The detailed analysis shall be discussed later by using models (e) and (f) in Figure 14. Incidentally, curve fitting by peak separation could not be achieved with high accuracy because too many overlapped absorption peaks belong to HA.

Figure 12 shows SALS patterns under polarization conditions observed for the pristine UHMWPE films and UHMWPE/HA

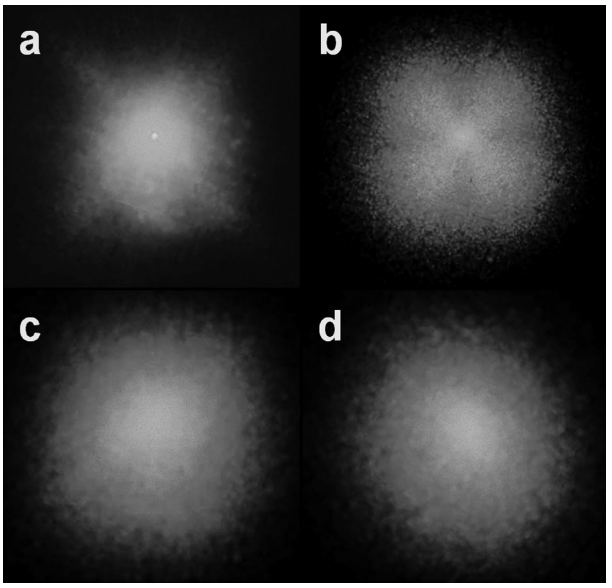

Figure 12. Hv light scattering patterns. (a) UHMWPE molded at 150 °C, (b) UHMWPE molded at 180 °C, (c) UHMWPE/HA composite (1.5 vol % HA) molded at 150 °C, (d) UHMWPE/HA composite (1.5 vol % HA) molded at 180 °C.

composites with 1.5 vol % HA content molded at 150 and 180 °C. The Hv patterns from pristine UHMWPE films molded at 150 and 180 °C show a circular type and a very dull X-type, respectively. The very dull X-type lobes in pattern (b) with maximum intensity at the center is due to the orientation fluctuations of the optical axes given as the correlation distance between two optical elements,[26,27] which is different from clear scattering from anisotropic rods.[47,48] The theory was proposed by Matsuo et al.[26] to analyze gel structures with optical anisotropy and is slightly different from the statistical approach proposed by Stein and Wilson.[25] In the proposed model system,[26] the difference between the polar and azimuthal angles of the principal axes of the i-th and j-th elements, which were defined with respect to the reference coordinate axis along the distance between two optically anisotropic elements, was given as a function of correlation distance between the two elements. The geometrical arrangement was represented in a previous paper.[26] The Hv scattered intensity from such a system can be obtained as follows

$$I_{\mathrm{Hv}} = K\delta^2 \int_0^{\pi}\int_0^{\infty} \mu'(r)\left\{\frac{1}{15}f(r) + g(r)(1 - f(r))\right.$$
$$\times\left[\frac{1}{720}(5\cos^4\alpha + 30\cos^2\alpha - 11) - \frac{1}{144}\cos^2\frac{\theta}{2}\right.$$
$$(5\cos^4\alpha + 6\cos^2\alpha - 3) + \frac{1}{576}\cos^4\frac{\theta}{2}\sin^2 2\mu$$
$$\left.\left.(35\cos^4\alpha - 30\cos^2\alpha + 3)\right]\right\}\cos[hr\cos\alpha]$$
$$r^2\sin\alpha\,dr\,d\alpha \qquad (5)$$

where θ and μ are the scattering and azimuthal angles of the scattered beam. α is the angle between r_{ij} and $h = (2\pi/\lambda)\mathbf{s}$, in which r_{ij} is the vector between the i-th and j-th volume

dx.doi.org/10.1021/am3030504 | ACS Appl. Mater. Interfaces 2013, 5, 1768–1780

elements and **s** is given by $\mathbf{s}_o - \mathbf{s}'$ ($\mathbf{s}_o$: incident beam, $\mathbf{s}'$: scattering vector). Here, $f(r)$ and $g(r)$ are the correlation functions associated with the polar and rotational angles in the coordinate concerning two optically anisotropic elements.[26] They are given by

$$f(r) = \exp\left(-\frac{r^2}{a^2}\right) \tag{6}$$

and

$$g(r) = \exp\left(-\frac{r^2}{b^2}\right) \tag{7}$$

where a and b are the correlation distances concerning orientation and rotational fluctuations between two optical axes with distance r, respectively, and they are generally described as parameters of a/λ and b/λ or b/a. λ is the wavelength in the medium. $\mu'(r)$, relating to the fluctuation of average polarizability, is independent of the shape of the scattering pattern because of no μ-dependence, while $g(r)$ and $f(r)$ are sensitive to the profile of the scattering pattern. If the correlation $g(r)$ for the rotational angle between two elements is zero, eq 5 reduces to

$$I_{Hv} = \frac{1}{15}K\delta^2 \int_0^\infty \mu'(r)f(r)\frac{\sinh r}{hr}r^2 dr \tag{8}$$

Equation 8 provides a circular pattern with no μ-dependence, which was derived by Stein and Wilson.[25] Incidentally, as shown patterns (c) and (d), the incorporation of a small amount of HA agglomerates provided a circular pattern indicating free rotation between two optical element axes as represented by eqs 5 and 8.

Figure 13 shows the scattering patterns calculated by using eq 5. The patterns on upper and lower sides are calculated at a/λ = 2 and 3, respectively. Through the numerical calculation, the patterns are found to be sensitive to the values of a/λ and b/a. The lobes of the calculated pattern become slightly duller with decreasing b/a, and then the pattern becomes close to a circular type. This indicates that the X-type pattern is attributed to the strong distance correlation for the rotational angle between two optically anisotropic elements. The patterns calculated at b/a = 1 and 3 were in good agreement with the patterns observed for pristine UHMWPE molded at 150 and 180 °C, respectively. This indicates that an X-type with the duller μ-dependence observed for UHMWPE molded at 180 °C indicates slightly strong correlation distance between optical elements, while the film molded at 150 °C has a weak correlation of crystallites for the rotational angle. Interestingly, the circular and X-type scattering patterns can elucidate (1) why the composites molded at 150 and 180 °C provided different morphology by SEM observation (Figure 14) and (2) why stress−strain curves of the specimens molded at 150 and 180 °C in Figure 8 are different.

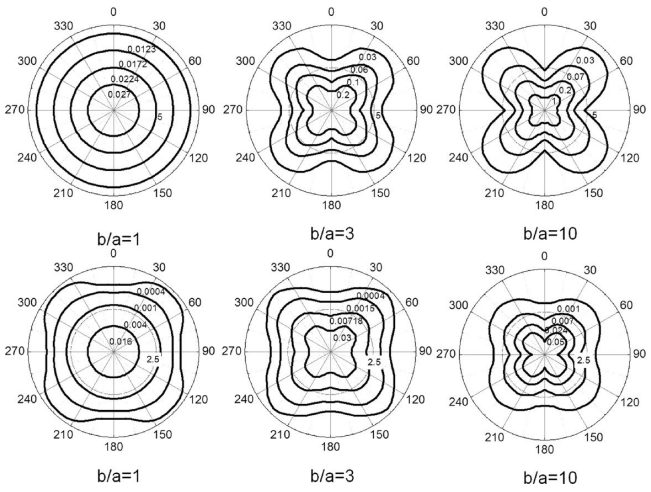

Figure 13. Hv light scattering patterns calculated by eq 5 as a function of b/a = 1, 3, and 10 at a/λ = 1 (upper side) and a/λ = 3 (lower side).

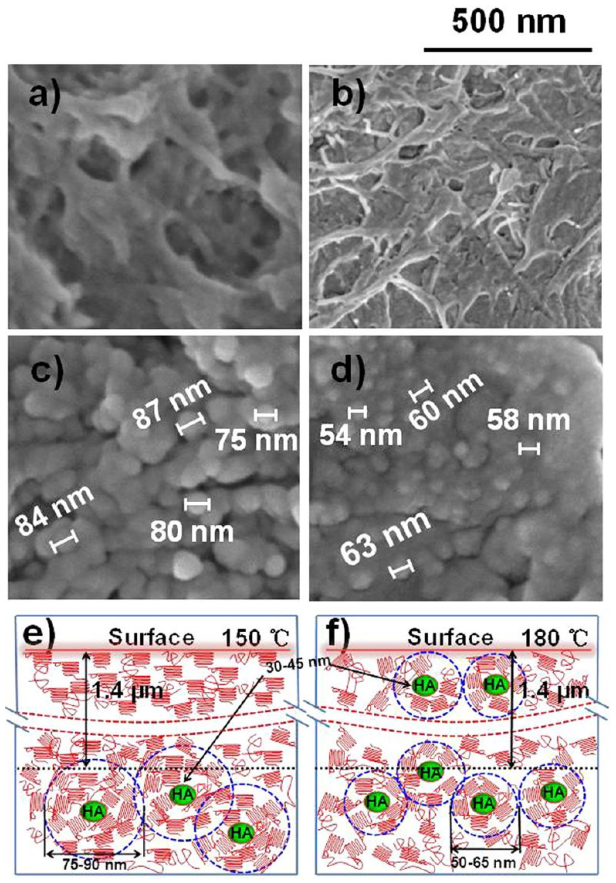

Figure 14. SEM images for cross-section area of pristine UHMWPE molded at 150 °C (a) and 180 °C (b) and UHMWPE/HA composites with 23.5 vol % HA content molded at 150 °C (c) and 180 °C (d). Models (e) and (f) are schematic designs for the cross-section of the UHMWPE/HA composites molded at 150 and 180 °C respectively.

Figure 14 shows SEM images of cross section for the pristine UHMWPE film and HA/UHMWPE composite molded at 150 and 180 °C, respectively. As for the pristine UHMWPE films, images (a) and (b) reveal that fibrous tissues formed by the gelation/crystallization process were maintained under the melting (molding) at 150 °C and recrystallization, while fibrous tissues became indistinct by melting (molding) at 180 °C and recrystallization. Hence, the X-type lobes of Hv pattern indicate that there exists strong rotational (azimuthal angle) correlation distance between two optical element axes concerning UHMWPE crystallites in the indistinct continuous UHMWPE fibrous tissues by melting at 180 °C. On the other hand, the correlation between optical elements in clear fibrous tissue is

very weak at 150 °C, since most crystalline fibrous tissues exist on HA surfaces without forming continuous film-like structures.

As shown in SEM images (c) and (d), the average size of UHMWPE/HA agglomerates in the composite molded at 150 °C were bigger than that in the composite at 180 °C. Judging from the supplemental SEM images in Figures 2 and 3, it may be expected that most of the HA agglomerates in the composite molded at 150 °C were covered by the UHMWPE layer. However, the UHMWPE layer on HA particles became thinner by partial flowing of UHMWPE chains when molding at 180 °C, and then the average size became slightly smaller. As discussed before, most of the melted UHMWPE chains were recrystallized on the surface of HA agglomerates, but the flowed off UHMWPE chains from the surface of HA agglomerates by molding at 180 °C were crystallized on the space area between UHMWPE/HA agglomerates.

Actually, as shown for gradient composites in Figure 4, the boundary lines could be observed clearly at 150 °C, while they could not be recognized at 180 °C

The crystallization of flowed off UHMWPE chains provided the formation of continuous films, and the films connect adjacent UHMWPE/HA agglomerates. Hence, as shown in Figure 8 and Table 2, most of the UHMWPE/HA agglomerates in the composite molded at 180 °C are connected to each other, and then the flexural yield stress, yield strain, maximum strain, and flexural modulus of the composites molded at 180 °C are higher than those of the composites molded at 150 °C. The formation of continuous films by partial melting at 180 °C has strong correlation distances for the azimuthal angels between two optical elements. This supports the indistinct X-type Hv pattern shown in Figure 12.

On the basis of a series of experimental results, the morphology of the composites molded at 150 and 180 °C can be represented as schematic designs (e) and (f), respectively. The models are proposed on the basis of SEM images (c) and (d) by considering WAXD profiles in Figure 9 and ATR spectra in Figure 11. To propose models (e) and (f) (in Figure 14) drawn by different scales, two units, μm and nm, were adopted, in which μm denotes depth distance from the surface containing a gap, while nm denotes average spherical agglomerate size.

As for the UHMWPE/HA composite molded at 150 °C, UHMWPE crystal chains existing on the surface layer (up to 1.4 μm depth from the surface) were oriented predominantly parallel to the resultant film surface because of the preferential orientation of the (110) plane on the surface, since most of the HA agglomerates did not exist in the surface layer. In contrast, UHMWPE crystal chains in UHMWPE/HA composites molded at 180 °C took a random orientation, and HA particles dispersed everywhere in the entire composite.

Furthermore, different from the molding at 180 °C, the flowing of melted UHMWPE chains at 150 °C fairly occurred, and then the diameter of the average spherical agglomerate size (ca. 75–90 nm) at 150 °C was bigger than the average diameter (50–65 nm) at 180 °C.

Certainly, the structure change by the difference of the molding temperatures, 150 or 180 °C, was sensitive to the mechanical properties of the composites. Returning to Figure 7, the frictional coefficient and wear resistance of the composite molded at 150 °C are superior to those of the composite melted at 180 °C as the acetabular cup. Such differences at 150 and 180 °C were strongly affected by the morphology on the sample surface layer but were hardly affected by crystallinity of the entire sample measured by DSC (see Table 1).

The shift of frictional coefficient maximum to higher load with increasing HA content (see Figure 7(a) and (b)) is obviously due to surface smoothness leading to the decreasing of the number of voids in the composite. To investigate the degree of sponge-like structure of the composites with increasing HA content, the Poisson's ratio is estimated by using a complex tensile modulus and shear modulus.

To obtain Poisson's ratio, it may be noted that very small external strain must be applied on the basis of infinitesimal deformation theory to satisfy the corresponding principle between elasticity and visco-elasticity of Hook's law, which is based on the different concept from large deformation for the bending in Figure 8.

The complex tensile and shear moduli measured for the composites molded at 150 and 180 °C were confirmed to be almost the same within the experimental error in spite of quite different morphology in Figure 4. Such a phenomenon sometimes has been observed for the composites whose particle contents are the same in the entire compositions. This is attributed to the very small external excitation to obtain a tensile modulus based on the infinitesimal deformation theory. Figure 15 shows temperature dependence on the

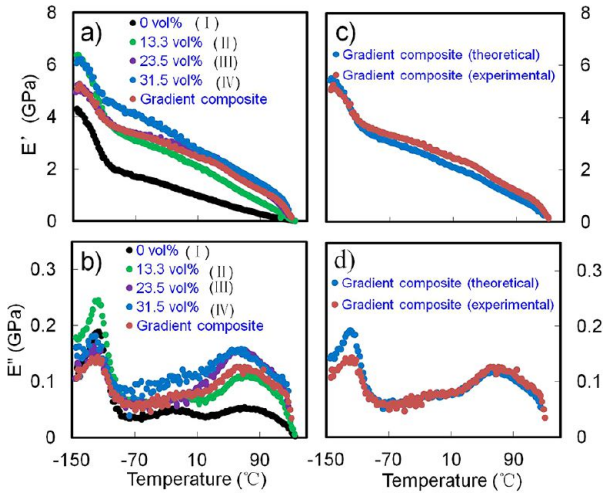

Figure 15. Left side: (a) temperature dependence of the storage tensile modulus E' and (b) loss tensile modulus E'' for UHMWPE/HA composites with the indicated HA contents. Right side: (c) temperature dependence of E' and (d) temperature dependence of E'' for the gradient composite, in which the theoretical data are calculated by eq A-1.

storage tensile modulus E' and loss tensile modulus E''. The measured temperature was in the range of −140–130 °C. The plots on the left side show the experimental results of each composite, and those on the right side show the comparison between experimental and theoretical results for the gradient composite shown in Figure 1(d). On the left side in Figure 16, the storage modulus (a) increases with increasing HA content. At 20 °C, the modulus at 31.5 vol % is about 2.5 GPa, which is more than 3 times of pristine UHMWPE. The imaginary part (b) has three dispersion peaks at −120, −20, and 60 °C corresponding to the γ, β, and α relaxations associated with the side group motion of amorphous chains, amorphous main chain motion, and crystal dispersion.[49−51] The theoretical calculation of the gradient composite on the right side was

dx.doi.org/10.1021/am3030504 | ACS Appl. Mater. Interfaces 2013, 5, 1768–1780

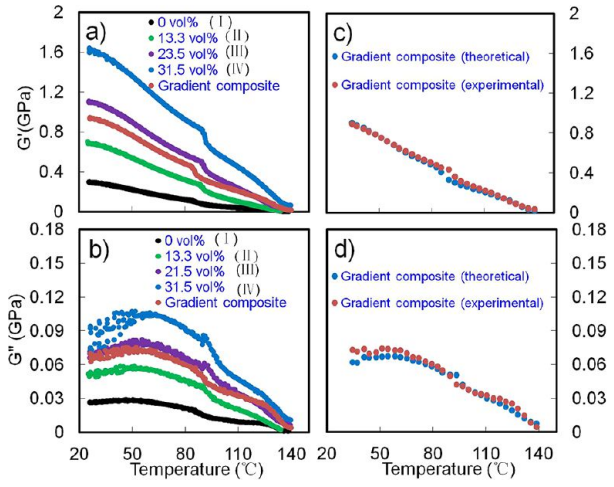

Figure 16. Left side: (a) temperature dependence of the storage shear modulus G' and (b) loss shear modulus G'' for UHMWPE/HA composites with the indicated HA contents. Right side: (c) temperature dependence of G' and (d) temperature dependence of G'' for the gradient composite, in which the theoretical data are calculated by eq A-2.

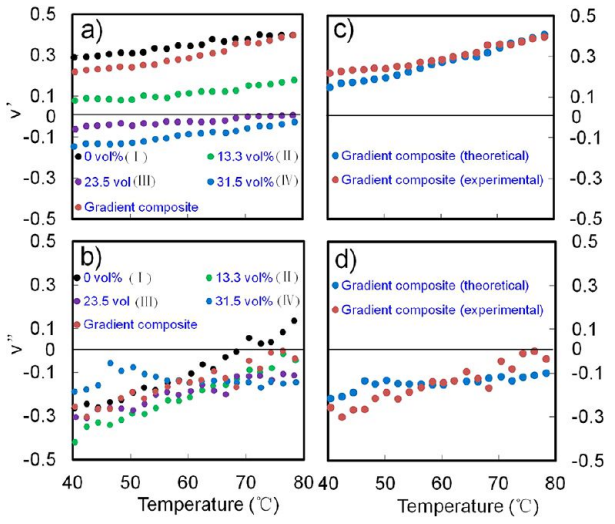

Figure 17. Left side: (a) temperature dependence of the real Poisson's ratio ν' and (b) imaginary Poisson's ratio ν'' or UHMWPE/HA composites with the indicated HA contents. Right side: (c) temperature dependence of ν' and (d) temperature dependence of ν'' for the gradient composite, in which the theoretical data are calculated by eq 9.

carried out by using eq A-1 in the Appendix. The theoretical curves for storage modulus E'_{GC} in frame (c) and loss modulus E''_{GC} in frame (d) calculated by the parallel model were in good agreement with the experimental curves, which ensured the smooth propagation of inner stress against external stress without avulsion on each boundary.

Figure 16 shows temperature dependence of the real G' and imaginary parts G'' for the composites in the temperature range 25−130 °C. The results on the left side show the experimental results, and those on the right side show the comparison between experimental and theoretical results for gradient composites shown in Figure 1(d). On the left side, the imaginary part (a) increases with increasing HA content, and the dispersion peak of the imaginary part (b) corresponding to the α relaxations is observed at around 60 °C similar to the behavior of E'' in Figure 15. The theoretical curves for E'_{GC} in frame (c) and E''_{GC} in frame (d) calculated by eq A-2 are in good agreement with the experimental curves for the gradient composite. The good agreement between experimental and theoretical results for E^* (= E' + E'') and G^* (= G' + G'') indicated high believability for the proposed parallel model.

Accordingly, it may be justified that the strains of isotropic phases I, II, III, and IV at each boundary as shown in Figure 1(d) are identical. As a result, it may be justified that the complex Poisson's ratio ν^*_{GC} of the gradient composite can be calculated by the following relationship.[24]

$$\nu^*_{GC} = \frac{E^*_{GC} - 2G^*_{GC}}{2G^*_{GC}} \tag{9}$$

Figure 17 shows the temperature dependence of complex Poisson's ratio for the individual UHMWPE/HA composites (phase I, II, III, and IV in Figure 1(d)) on the left side and shows the experimental and theoretical curves of the gradient composite on the right side. Each Poisson's ratio of phase I∼IV on the left-hand side is calculated by $\nu^*_P = (E^*_P - 2G^*_P)/2G^*_P$ (P = I, II, III, and IV). The real part ν' of complex Poisson's ratio close to room temperature for UHMWPE is ca. 0.3 indicating a normal value of crystalline plastics, and the value is beyond 0.4 at 60 °C indicating a rubbery state beyond α dispersion. With increasing HA content, the real part (a) becomes smaller and tends to be negative beyond 23.5 vol %, indicating the appearance of a pronounced spongy-like texture. The imaginary part ν'' in column (b) takes a negative value for the composites except the values of the pristine UHMWPE film beyond 70 °C, which is reasonable because $G'_P(E''_P + 2G''_P) < G''_P(E'_P + 2G''_P)$ for the composites. Anyway, it may be emphasized that the negative values justify the spongy-like structures observed by SEM observation in Figure 14.

As shown in the right side for the gradient composite, the calculated values of the real part (c) and imaginary part (d) are in good agreement with the experimental results, which justifies the application of infinitesimal deformation theory to model (d) in Figure 1.

The Poisson's ratio of each composite layer (I∼IV) reflects the deformation mechanism of spongy-like composites under normal load. The increase of negative Poisson's ratio in real part with increasing HA content indicates an increase in the number of voids in the spongy-like structure. Accordingly, the maximum of the friction coefficient shifted to higher normal load side with increasing HA content and attained 600 N for 31.5 vol % HA content (see Figure 7(a) and (b)). The decrease beyond the maximum is obviously thought to be due to the disappearance of a number of voids under high normal load, and it seems that the composite surface became markedly smooth.

A series of experimental analyses indicated that the friction coefficient and the wear resistance of the gradient composite molded at 150 °C are obviously better than those of the gradient composite molded at 180 °C, although the bending property is slightly poorer. The most important factor of the present study is to establish implant longevity of hip prosthesis in orthopedics. Accordingly, high wear resistance and smooth surface as bearing materials must be considered as the highest priority. In this viewpoint, the gradient composite prepared by gelation/crystallization seems to be the best as an acceptable cup.

4. CONCLUSION

The surface layer of the resultant composites ensured the excellent wear resistance and surface friction among the UHMWPE/HA composites which were prepared by the gelation/crystallization method and molded in the narrow temperature range 145−153 °C. The reason was analyzed in terms of morphological aspects. X-ray diffraction intensity from UHMWPE film revealed high preferential orientation of the (110) plane with the highest atom density of the PE crystal unit. FTIR (ATR) spectra from pristine UHMWPE films and UHMWPE/HA composites revealed that the existing probability of HA agglomerates on the surface layer (at ca. 1.4 μm depth) of the specimen molded at 150 °C was much lower than that molded at 180 °C, and the crystallinity of the thin layer was slightly higher. Furthermore, SEM observation and EDS spectra revealed that most of the HA agglomerates were covered by UHMWPE in the composites molded at 150 °C, while partially flowed off UHMWPE layers on the surface of HA agglomerates were observed at 180 °C. This means that UHMWPE chains under gelation were crystallized on the surface of HA agglomerates, but the partially flowed off UHMWPE chains from the surface of UHMWPE/HA agglomerates by molding at 180 °C were not recrystallized on the surface of HA agglomerates. The complex tensile moduli E^*, complex shear moduli G^*, and complex Poison's ratio ν^* were hardly affected by the molding temperatures, 150 or 180 °C. Poisson's ratio for the individual UHMWPE/HA composite and the gradient composite provided that the value became smaller with increasing HA content and tended to be negative beyond 23.5 vol % HA content, indicating an increase in voids in the spongy-like texture of the composites. Because of the descent degree of a number of voids in sponge-like tissues, surface fraction was smaller with increasing HA contents under high normal load. Of course, the frictional coefficient, wear rate, and bending properties prepared by gelation/crystallization were much superior to those prepared by a kneading method. A series of results suggested that by controlling molding temperature it turned out that the gradient composite prepared by the sol−gel method provides great merits as an acceptable cup of bearing material in an artificial joint.

APPENDIX

E^*_{GC} and G^*_{GC} of the gradient composite can be obtained by the concept that each layer lies adjacent to the other layer with the interface parallel to the external excitation direction, so that the strains of the two phases at the boundary are identical.[52,53] The four layers as shown in Figure 1(d) are adjacent to each other by the following process. Layers I and II are pasted together, and the resultant layer is named as layer α. Then layer α and layer III are pasted together. The resultant layer β is pasted together with layer IV finally. Through a series of the procedures, the complex tensile modulus E^* and the complex shear modulus G^* can be obtained by postulating stress hypothesis as follows

$$E^*_{GC} = \frac{1}{S^{\gamma*}_{11}} = \frac{\delta_3}{S^{\beta*}_{11}} + \frac{1-\delta_3}{S^{IV*}_{11}} + \frac{\left(\frac{S^{\beta*}_{12}}{S^{\beta*}_{11}} - \frac{S^{IV*}_{12}}{S^{IV*}_{11}}\right)^2}{\frac{S^{IV*}_{11}}{1-\delta_3}\left\{1-\left(\frac{S^{IV*}_{12}}{S^{IV*}_{11}}\right)^2\right\} + \frac{S^{\beta*}_{11}}{\delta_3}\left\{1-\left(\frac{S^{\beta*}_{12}}{S^{\beta*}_{11}}\right)^2\right\}} = E'_{GC} + iE''_{GC} \quad \text{(A-1)}$$

$$\frac{1}{G^*_{GC}} = \delta_3 S^{\beta*}_{44} + 2(1-\delta_3)(S^{IV*}_{11} - S^{IV*}_{12}) = \frac{1}{G'_{GC} + iG''_{GC}} \quad \text{(A-2)}$$

where $\delta_3 = 1/4$ and $S^{\beta*}_{ij}$ are complex compliance as follows

$$E^*_{\beta} = \frac{1}{S^{\beta*}_{11}} = \frac{\delta_2}{S^{\alpha*}_{11}} + \frac{1-\delta_2}{S^{III*}_{11}} + \frac{\left(\frac{S^{\alpha*}_{12}}{S^{\alpha*}_{11}} - \frac{S^{III*}_{12}}{S^{III*}_{11}}\right)^2}{\frac{S^{III*}_{11}}{1-\delta_2}\left\{1-\left(\frac{S^{III*}_{12}}{S^{III*}_{11}}\right)^2\right\} + \frac{S^{\alpha*}_{11}}{\delta_2}\left\{1-\left(\frac{S^{\alpha*}_{12}}{S^{\alpha*}_{11}}\right)^2\right\}} \quad \text{(A-3)}$$

$$S^{\beta*}_{44} = \delta_2 S^{\alpha*}_{44} + 2(1-\delta_2)(S^{III*}_{11} - S^{III*}_{12}) \quad \text{(A-4)}$$

$$\frac{1}{S^{\beta*}_{12}} = \frac{\delta_2}{S^{\alpha*}_{12}} + \frac{1-\delta_2}{S^{III*}_{12}} - \frac{\left(\frac{S^{\alpha*}_{11}}{S^{\alpha*}_{12}} - \frac{S^{III}_{11}}{S^{III*}_{12}}\right)^2}{\frac{S^{III*}_{12}}{1-\delta_2}\left\{\left(\frac{S^{III*}_{11}}{S^{III*}_{12}}\right)^2 - 1\right\} + \frac{S^{\alpha*}_{12}}{\delta_2}\left\{\left(\frac{S^{\alpha*}_{11}}{S^{\alpha*}_{12}}\right)^2 - 1\right\}} \quad \text{(A-5)}$$

where $\delta_3 = 1/4$ and $S^{\alpha*}_{ij}$ are complex compliance as follows

$$E^*_{\alpha} = \frac{1}{S^{\alpha*}_{11}} = \frac{\delta_1}{S^{I*}_{11}} + \frac{1-\delta_1}{S^{II*}_{11}} + \frac{\left(\frac{S^{I*}_{12}}{S^{I*}_{11}} - \frac{S^{II*}_{12}}{S^{II*}_{11}}\right)^2}{\frac{S^{II*}_{11}}{1-\delta_1}\left\{1-\left(\frac{S^{II*}_{12}}{S^{II*}_{11}}\right)^2\right\} + \frac{S^{I*}_{11}}{\delta_1}\left\{1-\left(\frac{S^{I*}_{12}}{S^{I*}_{11}}\right)^2\right\}} \quad \text{(A-6)}$$

$$S^{\alpha*}_{44} = \delta_1 S^{I*}_{44} + 2(1-\delta_1)(S^{II*}_{11} - S^{II*}_{12}) \quad \text{(A-7)}$$

dx.doi.org/10.1021/am3030504 | ACS Appl. Mater. Interfaces 2013, 5, 1768−1780

$$\frac{1}{S_{12}^{\alpha*}} = \frac{\delta_1}{S_{12}^{I*}} + \frac{1-\delta_1}{S_{12}^{II*}} - \frac{\left(\frac{S_{11}^{I*}}{S_{12}^{I*}} - \frac{S_{11}^{I*I}}{S_{12}^{II*}}\right)^2}{\frac{S_{12}^{II*}}{1-\delta_1}\left\{\left(\frac{S_{11}^{II*}}{S_{12}^{II*}}\right)^2 - 1\right\} + \frac{S_{12}^{I*}}{\delta_1}\left\{\left(\frac{S_{11}^{I*}}{S_{12}^{I*}}\right)^2 - 1\right\}} \quad \text{(A-8)}$$

where $\delta_1 = 1/2$.

AUTHOR INFORMATION

Corresponding Author

*E-mail: mm-matsuo@live.jp.

Notes

The authors declare no competing financial interest.

ACKNOWLEDGMENTS

The authors are indebted to Prof. Kenji Kawate, Department of Artificial joint and Regenerative Medicine, and Prof. Shigeyoshi Osaki, Department of Chemistry, of Nara Medical University, for their kind comments and cooperation. We would also like to thank TA Instruments company for shear modulus tests. This work was supported by the Natural Science Foundation of China (No. 21074016).

REFERENCES

(1) Mourad, A. H. I.; Fouad, H.; Elleithy, R. *Mater. Des.* **2009**, *30*, 4112−4119.
(2) Kanaga Karuppiah, K. S.; Bruck, A. L.; Sundararajan, S.; Wang, J.; Lin, Z. Q.; Xu, Z. H.; Li, X. D. *Acta Biomater.* **2008**, *4*, 1401−1410.
(3) Lahiri, D.; Dua, R.; Zhang, C.; de Socarraz-Novoa, I.; Bhat, A.; Ramaswamy, S.; Agarwal, A. *ACS Appl. Mater. Interfaces* **2012**, *4*, 2234−2241.
(4) Xu, L.; Chen, C.; Zhong, G. J.; Lei, J.; Xu, J. Z.; Hsiao, B. S.; Li, Z. M. *ACS Appl. Mater. Interfaces* **2012**, *4*, 1521−1529.
(5) Lerf, R.; Zurbrügg, D.; Delfosse, D. *Biomaterials* **2010**, *31*, 3643−3648.
(6) Ge, S. R.; Wang, S. B.; Gitis, N.; Vinogradov, M.; Xiao, J. *Wear* **2008**, *264*, 571−578.
(7) Saikko, V. *Wear* **1994**, *176*, 207−212.
(8) Kurtz, S. M.; Mazzucco, D.; Rimnac, C. M.; Schroeder, D. *Biomaterials* **2006**, *27*, 24−34.
(9) Shibata, N.; Tomita, N. *Biomaterials* **2005**, *26*, 5755−5762.
(10) Oral, E.; Wannomae, K. K.; Hawkins, N.; Harris, W. H.; Muratoglu, O. K. *Biomaterials* **2004**, *25*, 5515−5522.
(11) Roeder, R. K.; Sproul, M. M.; Turner, C. H. *J. Biomed. Mater. Res. A* **2003**, *67A*, 801−812.
(12) Haque, S.; Rehman, I.; Darr, J. A. *Langmuir* **2007**, *23*, 6671−6676.
(13) Joseph, R.; Tanner, K. E. *Biomacromolecules* **2005**, *6*, 1021−1026.
(14) Juhasz, J. A.; Best, S. M.; Brooks, R.; Kawashita, M.; Miyata, N.; Kokubo, T.; Nakamura, T.; Bonfield, W. *Biomaterials* **2004**, *25*, 949−955.
(15) Anderson, B. C.; Bloom, P. D.; Baikerikar, K. G.; Sheares, V. V.; Mallapragada, S. K. *Biomaterials* **2002**, *23*, 1761−1768.
(16) Fang, L. M.; Leng, Y.; Gao, P. *Biomaterials* **2006**, *27*, 3701−3707.
(17) Smolko, E.; Romero, G. *Radiat. Phys. Chem.* **2007**, *76*, 1414−1418.
(18) Xu, C.; Agari, Y.; Matsuo, M. *Polym. J.* **1998**, *30*, 372−380.
(19) Bin, Y.; Xu, C.; Zhu, D.; Matuo, M. *Carbon* **2002**, *40*, 195−199.
(20) Xi, Y.; Ishikawa, H.; Bin, Y.; Matsuo, M. *Carbon* **2004**, *42*, 1699−1706.
(21) Bin, Y. Z.; Kitanaka, M.; Zhu, D.; Matsuo, M. *Macromolecules* **2003**, *36*, 6213−6219.
(22) Suresh, S. *Science* **2001**, *292*, 2447−2451.
(23) Han, F. S.; Zhu, Z. G.; Liu, C. S.; Gao, J. C. *Damping behavior of foamed aluminum*; Springer: Boston, 1999; Vol. *30*, pp 771−776.
(24) Matsuo, M. *J. Chem. Phys.* **1980**, *72*, 899−910.
(25) Stein, R. S.; Wilson, P. R. *J. Appl. Phys.* **1962**, *33*, 1914.
(26) Matsuo, M.; Miyoshi, S.; Azuma, M.; Nakano, Y.; Bin, Y. Z. *Phys. Rev. E* **2005**, *72*, 1−10.
(27) Matsuo, M.; Luo, Y. L.; Galeski, A. *Phys. Rev. E* **2009**, *79*, 1−15.
(28) Chen, Q.; Bin, Y.; Matsuo, M. *Macromolecules* **2006**, *39*, 6528−6536.
(29) Bin, Y.; Yamanaka, A.; Chen, Q.; Xi, Y.; Jiang, X.; Matsuo, M. *Polym. J.* **2007**, *39*, 598−609.
(30) Xiong, L.; Xiong, D. S.; Jin, J. B. *J. Bionic Eng.* **2009**, *6*, 7−13.
(31) Gong, G. F.; Yang, H. Y.; Fu, X. *Wear* **2004**, *256*, 88−94.
(32) Al Twal, E. Q. H.; Chadwick, R. G. *J. Dent.* **2012**, *40*, 1044−1051.
(33) Sawatari, C.; Okumura, T.; Matsuo, M. *Polymer J.* **1986**, *18*, 741−758.
(34) Matsuo, M.; Sawatari, C. *Macromolecules* **1986**, *19*, 2036−2040.
(35) Agosti, E.; Zerbi, G.; Ward, I. M. *Polymer* **1992**, *33*, 4219−4229.
(36) Bruni, P.; Conti, C.; Corvi, A.; Rocchi, M.; Tosi, G. *Vib. Spectrosc.* **2002**, *29*, 103−107.
(37) Hagemann, H.; Snyder, R. G.; Peacock, A. J.; Mandelkern, L. *Macromolecules* **1989**, *22*, 3600−3606.
(38) Zerbi, G.; Gallino, G.; Del Fanti, N.; Baini, L. *Polymer* **1989**, *30*, 2324−2327.
(39) Xiong, L.; Xiong, D.; Jin, J. *J. Bionic Eng.* **2009**, *6*, 7−13.
(40) Wang, Q.; Liu, J.; Ge, S. *J. Bionic Eng.* **2009**, *6*, 378−386.
(41) Fang, L. M.; Leng, Y.; Gao, P. *Biomaterials* **2005**, *26*, 3471−3478.
(42) Fang, L. M.; Gao, P.; Leng, Y. *Composites, Part B* **2007**, *38*, 345−351.
(43) Nakashima, T.; Xu, C. Y.; Bin, Y. Z.; Matsuo, M. *Polym. J.* **2001**, *33*, 54−68.
(44) Sakai, Y.; Umetsu, K.; Miyasaka, K. *Polymer* **1993**, *34*, 318−322.
(45) Sakai, Y.; Miyasaka, K. *Polymer* **1988**, *29*, 1608−1614.
(46) Sakurada, I.; Kaji, K. *J. Polym. Sci., Part C: Polym. Symp.* **1970**, *31*, 57−76.
(47) Rhodes, M. B.; Stein, R. S. *J. Polym. Sci., Part A-2: Polym. Chem.* **1969**, *7*, 1539−1558.
(48) Matsuo, M.; Kakei, K.; Nagaoka, Y.; Ozaki, F.; Murai, M.; Ogita, T. *J. Chem. Phys.* **1981**, *75*, 5911−5924.
(49) Raff, R. A. V. *Encyclopedia of Polymer Science and Technology*; Wiley: New York, 1967; Vol. *6*, pp 275−332.
(50) Matsuo, M.; Sawatari, C.; Ohhata, T. *Macromolecules* **1988**, *21*, 1317−1324.
(51) Matsuo, M.; Bin, Y.; Xu, C.; Ma, L.; Nakaoki, T.; Suzuki, T. *Polymer* **2003**, *44*, 4325−4340.
(52) Matsuo, M. *Macromolecules* **1990**, *23*, 3261−3266.
(53) Matsuo, M.; Sawatari, C.; Iwai, Y.; Ozaki, F. *Macromolecules* **1990**, *23*, 3266−3275.